

# The high-velocity outflow in the proto-planetary nebula Hen 3–1475 <sup>\*</sup>

A. Riera<sup>1,2</sup>, P. García-Lario<sup>3</sup>, A. Manchado<sup>4,5</sup>, M. Bobrowsky<sup>6</sup>, and R. Estalella<sup>2</sup>

<sup>1</sup> Departament de Física i Enginyeria Nuclear, Universitat Politècnica de Catalunya, Av. Víctor Balaguer s/n, E-08800 Vilanova i la Geltrú, Spain e-mail: [angels.riera@upc.es](mailto:angels.riera@upc.es)

<sup>2</sup> Departament d’Astronomia i Meteorologia, Universitat de Barcelona, Av. Diagonal 647, E-08028 Barcelona, Spain

<sup>3</sup> ISO Data Centre. Science Operations and Data Systems Division. Research and Scientific Support Department of ESA. Villafranca del Castillo. Apartado de Correos 50727. E-28080 Madrid, Spain

<sup>4</sup> Instituto de Astrofísica de Canarias, E-38200 La Laguna (Tenerife), Spain

<sup>5</sup> Consejo Superior de Investigaciones Científicas, Spain

<sup>6</sup> Challenger Center for Space Science Education. 1250 North Pitt Street, Alexandria, VA 22314, USA

Received October 30, 2002; accepted February 13, 2003

**Abstract.** The proto-planetary nebula Hen 3–1475 shows a remarkable highly collimated optical jet with an S-shaped string of three pairs of knots and extremely high velocities. We present here a detailed analysis of the overall morphology, kinematic structure and the excitation conditions of these knots based on deep ground-based high dispersion spectroscopy complemented with high spatial resolution spectroscopy obtained with STIS onboard HST, and WFPC2 [N II] images. The spectra obtained show double-peaked, extremely wide emission line profiles, and a decrease of the radial velocities with distance to the source in a step-like fashion. We find that the emission line ratios observed in the intermediate knots are consistent with a spectrum arising from the recombination region of a shock wave with shock velocities ranging from 100 to 150 km s<sup>-1</sup>. We propose that the ejection velocity is varying as a function of time with a quasi-periodic variability (with timescale of the order of 100 years) and the direction of ejection is also varying with a precession period of the order of 1500 years. Some slowing down with distance along the axis of the Hen 3–1475 jet may be due to the entrainment process and/or to the environmental drag. This scenario is supported by geometric and kinematic evidence: firstly, the decrease of the radial velocities along the Hen 3–1475 jet in a step like fashion; secondly, the kinematic structure observed in the knots; thirdly, the point-symmetric morphology together with the high proper motions shown by several knots; and finally the fact that the shock velocity predicted from the observed spectra of the shocked knots is much slower than the velocities at which these knots move outwards with respect to the central source.

**Key words.** ISM: jets and outflows — planetary nebulae: kinematics — planetary nebulae: individual: Hen 3–1475

## 1. Introduction

Hen 3–1475 is a highly collimated bipolar proto-planetary nebula (PPN, hereafter), which displays a spectacular S-shaped string of point-symmetric knots extending over 17'' along its main axis. It was first observed from the ground

by Riera et al. (1995, hereafter R95) and from the ground and space by Bobrowsky et al. (1995) and by Ueta et al. (2000), and identified as a massive post-AGB star rapidly evolving into the planetary nebula (PN, hereafter) phase. More recently, with the help of HST WFPC2 observations, it has been possible to resolve the subarcsecond structure of the outer knots and of the inner region of this extremely complex source (Borkowski et al. 1997).

Hen 3–1475 was recognized for the first time as a transition object in the post-AGB phase by Parthasarathy & Pottasch (1989) from the analysis of its far infrared IRAS colours. Later, it was revealed as a highly collimated bipolar PPN by R95, showing the highest outflow velocity ever observed for a PPN and a peculiar point-symmetric morphology consisting of pairs of knots symmetrically distributed with respect to the central star. From the ob-

*Send offprint requests to:* A. Riera

<sup>\*</sup> Based on observations made during service time with the 2.5 m Isaac Newton Telescope operated on La Palma by the Isaac Newton Group of Telescopes in the Spanish Observatorio del Roque de los Muchachos of the Instituto de Astrofísica de Canarias, and observations made with the Hubble Space Telescope, obtained from the Data Archive at the Space Telescope Science Institute, which is operated by the Association of Universities for Research in Astronomy, Inc., under NASA contract NAS5-26555

served spectra, together with the detection of highly supersonic velocities, it was concluded that the emission in the outer knots was produced in a shock which propagates through a nitrogen-enriched medium (R95).

A velocity gradient decreasing from  $900 \text{ km s}^{-1}$  in the innermost region close to the central star down to  $450 \text{ km s}^{-1}$  in the outer knots was also found. This was interpreted as a sign of variability of the ejection velocity by R95 and Riera et al. (2001,2002). However, Borkowski & Harrington (2001; BH01, hereafter) interpret this velocity gradient in a different way, as a sign of efficient deceleration of the jet by a much slower bipolar outflow. BH01 also suggest that the wide line profiles observed in the knots are a sign of violent deceleration of the jet.

An inclination angle of the bipolar outflow of  $50^\circ$  with respect to the plane of the sky, was derived by BH01 from the Doppler shifts of the scattered stellar  $H\alpha$  line, considering that the reflected light is redshifted due to the motion of the dust away from the star, and that the  $H\alpha$  emission is also red- or blueshifted as a consequence of the inclination of the flow.

The strong far infrared excess detected by IRAS can be identified as the remnant emission from the dust grains formed in the circumstellar shell during the previous strong mass loss AGB phase, while the current presence of strong P-Cygni profiles in the Balmer lines indicates that mass loss is still on-going (although at a much lower rate). This is confirmed by the detection of thermal emission from hot dust in the near infrared (García-Lario et al. 1997).

The nitrogen overabundance derived from the optical spectroscopy (R95) and the high luminosity ( $> 10^4 L_\odot$  at a distance of 5.8 kpc - as explained below) suggest a high mass progenitor for the central star of Hen 3–1475.

Sánchez Contreras & Sahai (2001) have recently analysed two blue-shifted absorption features detected in the light of  $H\alpha$  arising from a region very close to the central source using STIS data. They detect the presence of two different winds both with a kinematic age of only tens of years: a fast wind (flowing with velocities  $\sim 150 - 1200 \text{ km s}^{-1}$ ) and an ‘ultrafast’ wind which is flowing with velocities up to  $2300 \text{ km s}^{-1}$ . Sánchez Contreras & Sahai (2001) find that the ‘ultrafast’ wind is highly collimated (at distances  $\sim 10^{16} \text{ cm}$ ) in a direction which differs from previous mass ejection axes and shows a large velocity gradient. This ‘ultrafast’ wind is identified as a ‘pristine’ post-AGB outflow which has not yet been altered by its interaction with the AGB envelope.

VLA observations revealed the presence of a compact radio continuum source close to the central star (Bobrowsky et al. 1995, Knapp et al. 1995), indicating that the central star has already become hot enough to ionize the gas in its vicinity.

The presence of a large amount of neutral gas in the envelope has also been detected with the help of observations in the light of the CO molecule emission as an expanding torus of material (Knapp et al. 1995, Bujarrabal et al. 2001). In addition, Hen 3–1475 exhibits strong OH maser

emission (te Lintel Hekkert 1991; Bobrowsky et al. 1995). Both CO and OH emission show a broad ( $60 \text{ km s}^{-1}$ ) profile indicative of a fast molecular outflow which appears to be extended ( $2''$ ). Bujarrabal et al. (2001) identify in the wide CO profile two different components: a slow component (with an expansion of  $\sim 7 \text{ km s}^{-1}$ ) and a fast outflow, which is assumed to be bipolar in the direction of the nebular axis. Similarly, the OH emission profile consists of a plateau of emission and sharp peaks at  $+21.5$  and  $+70.9 \text{ km s}^{-1}$ , implying an expansion velocity of at least  $25 \text{ km s}^{-1}$  in the outer parts of the neutral envelope. The blueshifted and redshifted peaks are displaced  $1''$  in the direction of the optical jet, which suggest an aspherical shell. It is remarkable that the OH radial velocity increases linearly with distance to the source, a situation that has been observed in other PPNe, and can be explained in terms of bipolar winds (Zijlstra et al. 2001).

In this paper we present a detailed analysis of the kinematics of the high-velocity outflow based on new ground-based spectroscopic data taken in the wavelength range corresponding to the [O I] 6300 Å, [N II] 6548, 6584 Å,  $H\alpha$ , and [S II] 6717, 6731 Å emission lines, covering  $\pm 9''$  NW and SE of the central star. This is complemented with the high spatial resolution information provided by the Space Telescope Imaging Spectrograph (STIS) data. Based on this new comprehensive data set we re-discuss the overall kinematics and the excitation of the knots observed in Hen 3–1475.

In Sect. 2 we describe the observations on which our analysis is based, while in Sect. 3 we present the improved results obtained on the morphology description and the kinematic properties of the knots. Possible excitation mechanisms for the lines observed and several different scenarios which could be responsible for the complex high velocity field associated to Hen 3–1475 are discussed in Sect. 4 in connection with the nature and evolutionary stage of the central source, while our main conclusions are presented in Sect. 5.

## 2. Observations

### 2.1. HST images

Two sets of high spatial resolution optical WFPC2 images of Hen 3–1475 taken at different epochs with HST on 1996 June 6 and 1999 September 19 were used to study the overall morphology of the source and to measure the proper motion of the knots. The images were obtained in both cases with the Planetary Camera ( $800 \times 800$  pixels with a plate scale of  $0''.0455 \text{ pixel}^{-1}$ ) and through the F658N narrow filter ( $\lambda_c = 6590 \text{ Å}$ ;  $\Delta\lambda = 28.5 \text{ Å}$ ). The images taken in 1996 were originally part of Cycle 6 proposal 6347 (P.I.: K.F. Borkowski), while the 1999 images were part of Cycle 7 proposal 7285 (P.I.: J.P. Harrington). These images went through the pipeline processing at the Space Telescope Science Institute. After HST pipeline cal-

ibration the cosmic rays were removed using the “crrej” task within the IRAF<sup>1</sup> package.

## 2.2. High resolution optical spectroscopy

Two complementary spectroscopic data sets are combined in this work: (i) deep ground-based long slit optical spectroscopy along the bipolar axis with high spectral resolution ( $R \sim 20,000$ ) and (ii) spectroscopy with very high spatial resolution along the bipolar axis obtained with STIS (Space Telescope Imaging Spectrograph) onboard HST.

### 2.2.1. Ground-based spectroscopy

The ground-based long slit optical spectra of Hen 3–1475 were obtained in June 1998 as part of the Isaac Newton Group service program using the Intermediate Dispersion Spectrograph (IDS) equipped with the 500 mm camera and a TEK CCD installed at the Cassegrain focus of the 2.5 m (f/15) Isaac Newton Telescope at the Observatorio del Roque de los Muchachos (La Palma, Spain). The slit width used was 2", oriented along the major axis of the bipolar nebula passing through the central star at a P.A. of 135°, covering not only the innermost and intermediate knots but also grazing the outer knots.

Two exposures, each one covering a different spectral range, were performed with the high resolution grating H1800V centered at 6640 Å and at 6300 Å respectively, yielding a spectral sampling of 0.46 Å, equivalent to a velocity resolution of 21 km s<sup>-1</sup>. The spatial sampling is 0".33 pixel<sup>-1</sup> in both cases. With the first exposure ( $\lambda_c = 6640$  Å) we covered the [N II] 6548, 6584 Å, H $\alpha$  and [S II] 6717, 6731 Å emission lines, while the second exposure ( $\lambda_c = 6300$  Å) was intended to cover the [O I] 6300 Å emission line, which is of great importance in determining the excitation mechanisms involved. The exposure times were 900 and 1800 s for the first and second exposures, respectively, improving the S/N ratio of previous observations (R95) and extending the observations up to a distance of  $\pm 9'$  from the central star. This meant that, for the first time, we were able to study the kinematic structure of the complete outflow.

Individual spectra were corrected for bias, flat-field and cosmic ray events, and were calibrated in wavelength using the standard tasks for long-slit spectroscopy within the IRAF package. The spectra were not flux calibrated.

### 2.2.2. HST spectroscopy

STIS data were retrieved from the HST Data Archive. Long-slit spectra were obtained with the STIS slit oriented along the bipolar axis of Hen 3–1475 on 1999 June 15–16. They were originally part of Cycle 7 proposal 7285 (P.I.:

J.P. Harrington). The spectrograph slit had a projected length of 52". The G750M grating, centered at  $\lambda_c = 6581$  Å, was used, covering the wavelength region including [O I] 6300 Å, [N II] 6548, 6584 Å, H $\alpha$  and [S II] 6717, 6731 Å. A 0".1 slit width was used, giving a spectral resolution of  $\sim 50$  km s<sup>-1</sup> and a dispersion of 0.56 Å pixel<sup>-1</sup>. The spatial sampling was 0".05.

Spectra were obtained at nine parallel positions with increasing offsets with respect to the central star of 0".1 at both sides of the nebula from  $-0".4$  to  $+0".4$ . The central spectra (offsets  $-0".1$ ,  $0".0$ , and  $+0".1$ ) cover the bright innermost regions (including the knots named NW1 and SE1; see Fig. 1). The spectra with  $+".2$  to  $+".4$  displacements from the central star position partially covered the SE2 knot with the slit at its western edge, but the blue-shifted NW2 knot was unfortunately missed (see Fig. 1). They all were calibrated at the Space Telescope Science Institute following the HST pipeline calibration (see BH01 for a detailed description).

Other authors have previously reported in the literature some of the results derived from the analysis of this STIS spectroscopy. BH01 had their main interest in the study of the scattered emission in order to determine the inclination of the jet axis. Based on the same data set, Sánchez Contreras & Sahai (2001) have recently presented a detailed study of the high velocity wind from the central star at the innermost regions of the nebula. However, the STIS spectra arising from the knots have not yet been discussed in detail. As we will discuss later, long-slit STIS spectra confirm previous results reported in the literature but also contain interesting new information about the high-velocity bipolar outflow, never discussed before, illustrating the changes in the line profiles and radial velocities along the flow with unprecedented spatial resolution.

## 3. Results

### 3.1. Morphology of the outflow

The images taken with HST using the narrow F658N filter essentially trace the ionized gas in Hen 3–1475 through the detection of the nebular emission coming from the [NII] 6584 Å line. However, it should be noted that losses are expected in the detection of this line from the more extremely blueshifted regions of the nebula, not covered by the filter, due to the extremely large velocities involved. Moreover, extremely redshifted H $\alpha$  emission is also expected to contribute to the emission detected through this filter in the inner regions of the redshifted lobe, making more difficult a straightforward interpretation of the surface brightness distribution observed in the HST images.

In Fig. 1 we show as an example one of the F658N images taken in 1999 where we can see the jet-like structure of Hen 3–1475 and three pairs of symmetric emission knots, named following the nomenclature used by Borkowski et al. (1997). The overall shape looks very similar to that observed in the images taken in 1996. From these images Borkowski et al. (1997) remarked on the

<sup>1</sup> IRAF is distributed by the National Optical Observatories, which is operated by the Association of Universities for Research in Astronomy, Inc., under contract with the National Science Foundation.

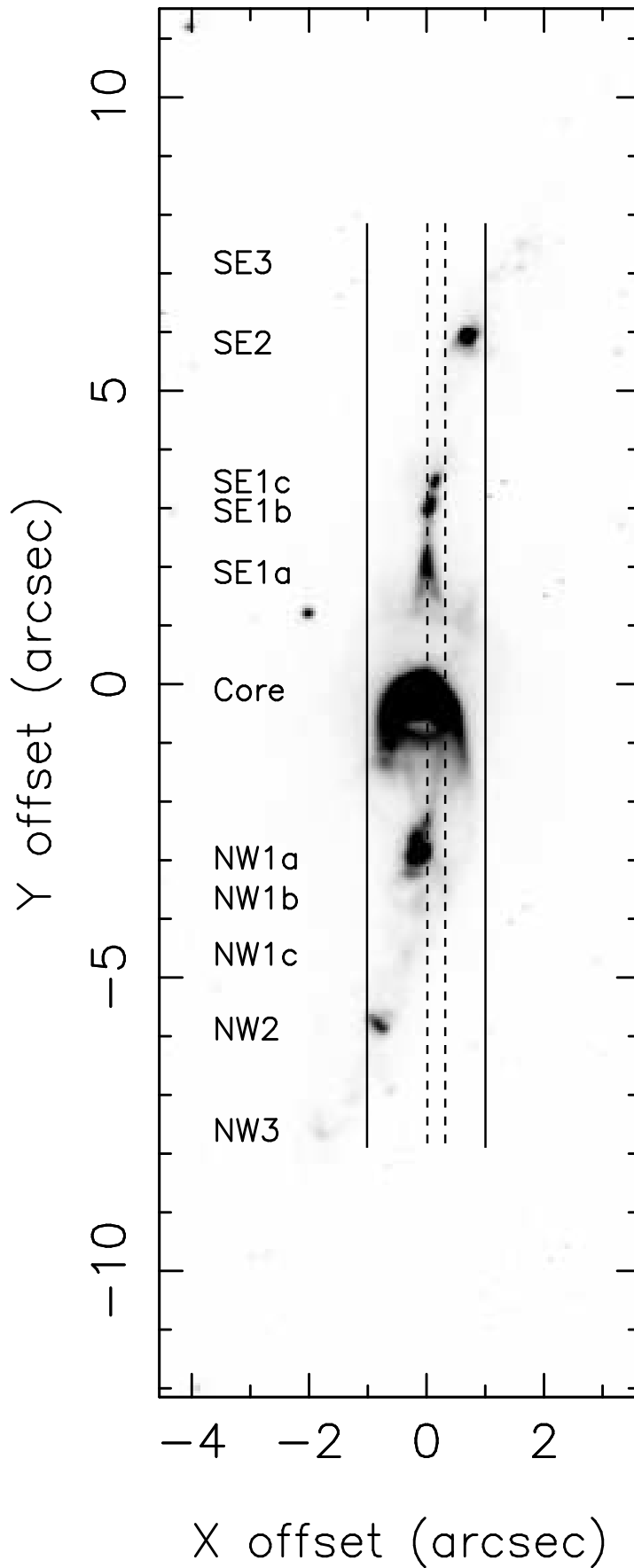


**Fig. 1.** HST image of Hen 3–1475 taken through the F658N filter which essentially traces the emission from the [N II] 6584 Å, derived from the 1999 observations. The (0,0) position was set at the location of the core, where the maximum emission was measured. The slit position used for the ground-based observations (with a width of 2'') is shown by two

presence of three pairs of well-collimated knots and the presence of converging funnel-shaped structures connecting the innermost knots and the core region in the NW and SE lobes, which are still clearly visible in the 1999 images.

The knots SE1 and NW1 show subarcsecond structure, with the existence of three well defined compact subcondensations which are labelled with a letter after the number (see Fig. 1). The three subcondensations of the SE1 knot show similar intensities in the emission line images and are located at distances of  $2''.27$ ,  $3''.29$  and  $3''.65$  from the central core. In the NW knot the subcondensations NW1b and NW1c are much fainter than NW1a in the emission line images (see Fig. 1). However, these substructures are much more prominent in scattered light (Riera et al. 2001). Subcondensations NW1a, NW1b and NW1c are located at larger angular distances from the central core than their SE counterparts. NW1a is located at  $2''.60$  from the central source, while the NW1b and NW1c are located at  $3''.46$  and  $4''.36$ , respectively. This is most probably a projection effect. Assuming that the location of the NW1 and SE1 knots is symmetric with respect to the central source, the difference between the projected distances for each subcondensation and its counterpart, can be explained if the jet is not coplanar. In this case, a difference  $\Delta i = i_{NW} - i_{SE} < 10^\circ$ , where  $i_{NW}$  and  $i_{SE}$  are the inclination angles of the NW and SE sides of the jet, would explain the discrepancy between the projected distances from the central source to the NW1 subcondensations and the SE1 counterparts.

As it was already proposed in R95, the S-shaped morphology of the jet of Hen 3–1475 suggests that the direction of ejection is not constant. If these variations are interpreted as a consequence of precession, the observed morphology can be fitted with a precession angle  $< 10^\circ$  and a period of  $\sim 1500$  years (as quoted by R95).

### 3.2. Determination of the systemic velocity

The systemic velocity of Hen 3–1475 can be estimated assuming that the velocity field of the knots is symmetric about the central source, so that the velocity is the same for the redshifted and blueshifted knots of each pair. This way, from our IDS ground-based spectra, we derive the value of  $+44 \text{ km s}^{-1}$  both from the outermost (NW3 and SE3) and from the middle (NW2 and SE2) knots. This velocity is consistent within the errors with the value of  $+40 \text{ km s}^{-1}$  reported by BH01 from the circumstellar FeII emission lines and it is also close to the velocity centroid of the OH 1667 MHz emission, which is  $+46 \text{ km s}^{-1}$  (Bobrowsky et al. 1995; Zijlstra et al. 2001) and the systemic velocity of  $+48 \text{ km s}^{-1}$  determined from the CO profiles (Bujarrabal et al. 2001). In the following we will adopt a local standard of rest (LSR) systemic velocity of  $+44 \text{ km s}^{-1}$ .

### 3.3. Kinematics of the outflow

The spatially resolved kinematic information contained in our ground-based spectroscopy, combined with the STIS observations, has been used to fully map for the first time the velocity of the gas along the bipolar axis of Hen 3–1475 over the whole extension of the nebula.

For this, we have followed the standard method of fitting multiple gaussians to the observed emission line profiles observed in our ground-based spectroscopy (fitting was done using standard IRAF packages) and transforming the derived central wavelengths of each individual line into LSR velocities.

These fits have been obtained for the [N II] 6584, 6584 Å, H $\alpha$ , [S II] 6717, 6731 Å and [O I] 6300 Å emission lines. Fig. 2 shows the position-velocity diagrams derived from [N II] 6584 Å, and [O I] 6300 Å emission lines. The results obtained using different forbidden emission lines are consistent each other within the errors and they are all also very similar to those obtained in the light of H $\alpha$  (not shown in Fig. 2). The position-velocity diagrams of H $\alpha$  and [S II] 6717 Å were shown in Riera et al. (2001, 2002).

Note that the [O I] emission lines observed in the central region show very low associated velocities which correspond to reflected emission originated in the central region which is being scattered by dust particles (labeled as ‘core’ in Fig. 2). The kinematic pattern of the scattered light, also observed in H $\alpha$ , has already been discussed by Riera et al. (2001) (based on ground-based spectra) and BH01 (based on the STIS spectra), and will not be further discussed here. In all these diagrams the position of the central source is identified with the centroid of the spatial distribution (along the slit) of the H $\alpha$  and [O I] 6300 Å emission, which is located at  $0''.0$ .

In Fig. 3 we show the kinematic structure of the innermost regions of the nebula derived from the STIS measurements corresponding to slit positions along the bipolar axis at angular distances of  $-0''.1$ ,  $0''.0$ , and  $+0''.1$  from the central source in the light of [N II] 6548, 6584 Å and H $\alpha$ . These observations covered completely the innermost SE1 and NW1 knots (see Fig. 1). Extraordinary line widths, up to  $\simeq 1050 \text{ km s}^{-1}$ , are clearly visible in the position-velocity diagram of these knots along with remarkable double-peaked profiles.

Similarly, in Fig. 4 we show in detail the sub-structure of the SE2 knot as observed with STIS. In this case, the velocity-position diagram shows the combined information extracted from the exposures taken with the slit positions  $+0''.2$ ,  $+0''.3$ , and  $+0''.4$  in the light of H $\alpha$  and [N II] 6584 Å only. Again we can see clearly the presence of remarkable double-peaked profiles, which were previously reported by R95.

Fig. 3 shows weak emission in the region between the core and NW1a at a distance of  $1''.8$  from the central source which corresponds to the converging funnel-shaped structures connecting the innermost knots and the core region seen in the emission line images (see Fig. 1). There is

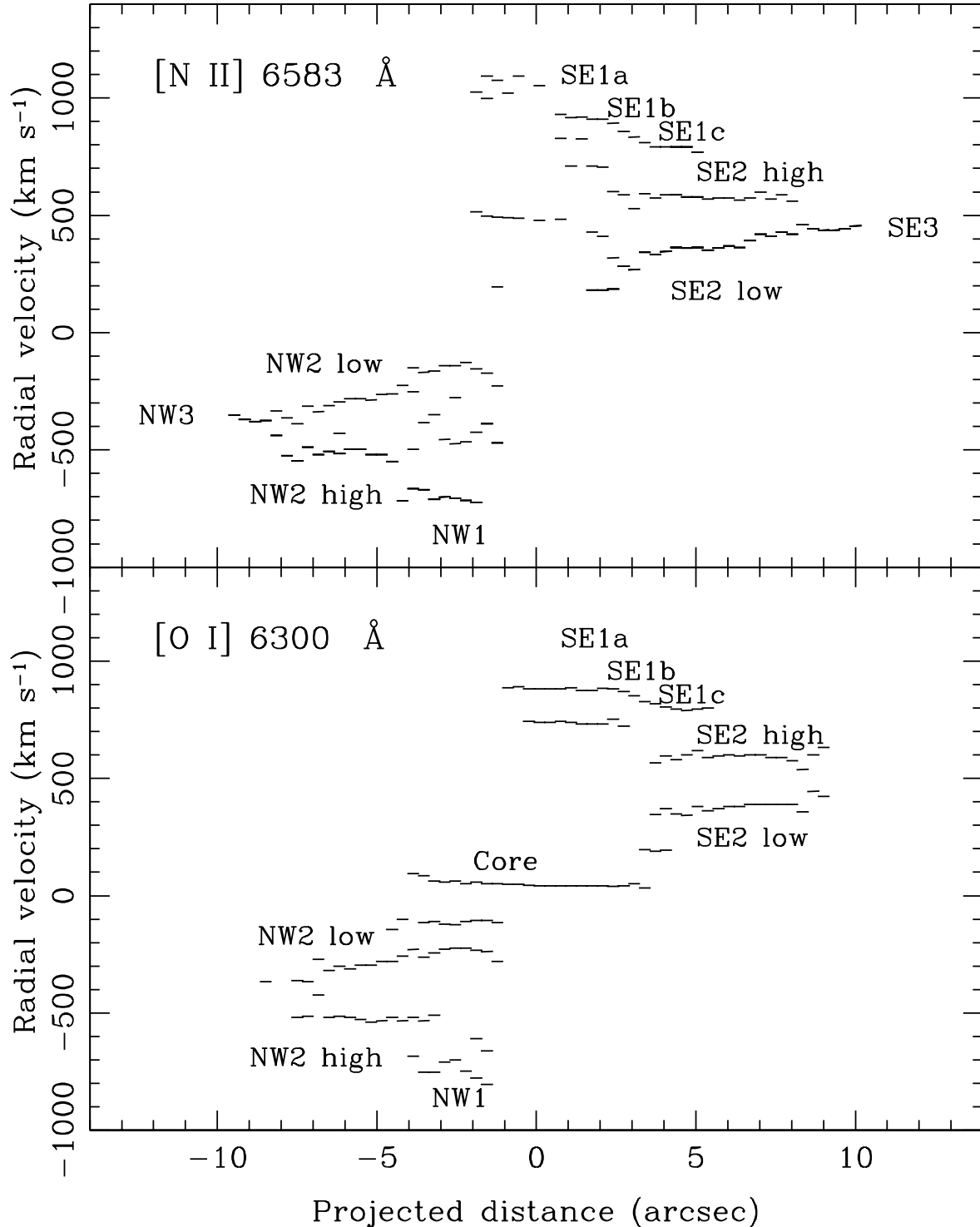


**Fig. 2.** Relative radial velocity *vs.* distance to the central source along the axis of the nebula for [N II] 6584 Å (*upper panel*) and [O I] 6300 Å (*lower panel*). Relative velocities are quoted with respect to the systemic radial velocity (= 44 km/s). The labels identify the position of the different components of the knots. The ‘low’ and ‘high’ levels identify the low and high-velocity components shown by the intermediate knots. In the lower panel the label ‘core’ accounts for the scattered [O I] emission arising from the central core

some contribution of scattered light from the strong H $\alpha$  emission from the central source, but part of the observed emission is intrinsic to the jet. The emission lines formed in this region show asymmetric broad single-peaked emis-

sion line profiles, moving at  $-920$  km s<sup>-1</sup> with respect to the systemic velocity and with a redward tail up to  $-500$  km s<sup>-1</sup>.

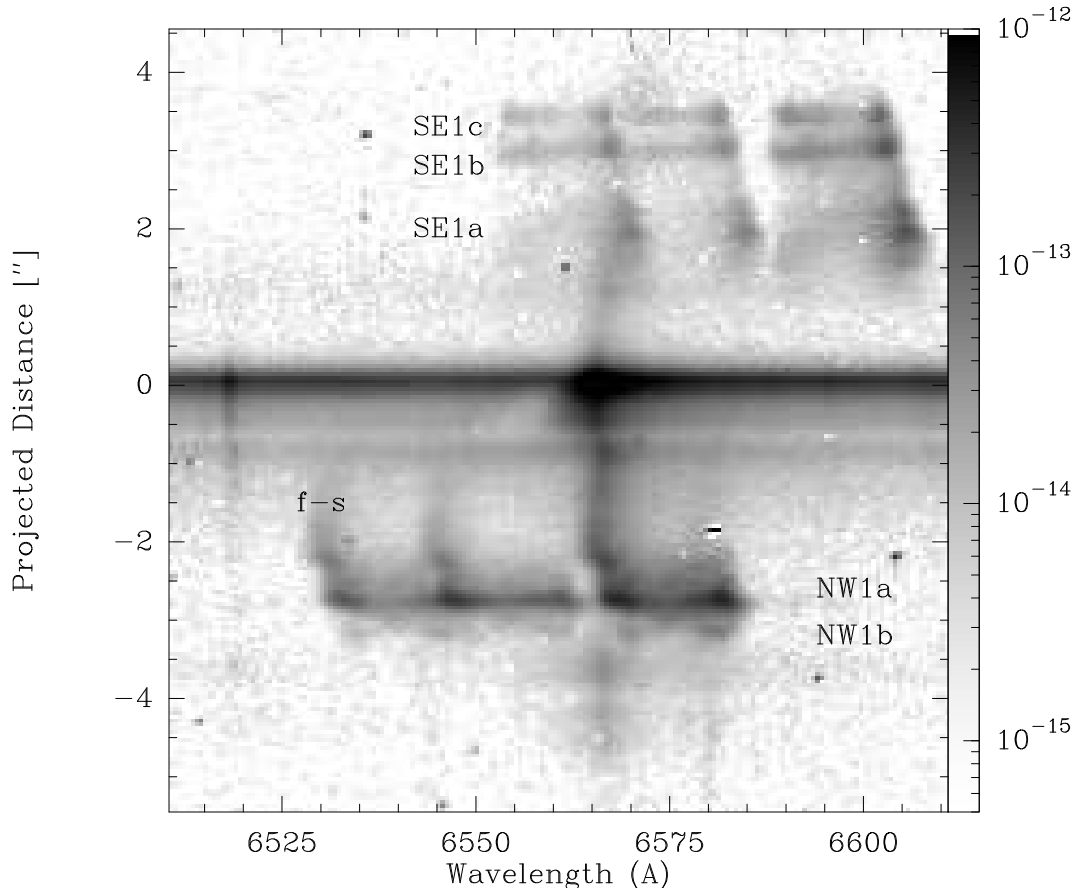


**Fig. 3.** Position-velocity diagram for  $[\text{N II}]$  6548, 6584 Å, and  $\text{H}\alpha$  6563 Å obtained with STIS at slit positions with offsets  $-0''.1$ ,  $0''.0$  and  $+0''.1$  with respect to the central source. We have used a logarithmic grey scale. The grey bar indicates the flux value in  $\text{erg cm}^{-2} \text{s}^{-1} \text{Å}^{-1}$ . The ordinate gives the position along the spectrograph slit. The main features have been identified with a label. The structures labelled as “f-s” are the funnel-shaped features (see text).

One of the most remarkable results found in the analysis of this outflow is the decrease in radial velocity when moving outwards along the jet. Within the knot NW1, we observe an abrupt decrease of  $145 \text{ km s}^{-1}$  in just  $0''.875$  (see Fig. 3). The high-velocity peak of NW1a (at  $2''.6$  from the central source) occurs at  $-766 \text{ km s}^{-1}$ , while at  $3''.2$  from the central source (close to NW1b) the emission peak is at  $-720 \text{ km s}^{-1}$ .

We also see rapid velocity changes within SE1 in the transition regions from each subcondensation to the next one. The strongest emission occurs in the high-velocity component, which is centered at  $\simeq +890$  (SE1a) to  $+740$  (SE1c)  $\text{km s}^{-1}$ . The radial velocity decreases outwards in a step-like fashion, with an abrupt decrease of  $112 \text{ km s}^{-1}$  in the transition from SE1a to SE1b and a decrease of  $36 \text{ km s}^{-1}$  in the transition from SE1b to SE1c. Further out (i.e. at larger distances from the central source) the observed radial velocities also decrease with distance.

Fig. 2 clearly illustrates the decrease of the radial velocities with increasing distance to the source, and the change of  $\sim 300 \text{ km s}^{-1}$  in the radial velocity from the innermost regions to the intermediate knots. The radial velocity also decreases, although only by  $\sim 50 \text{ km s}^{-1}$ , from the intermediate knots NW2 and SE2 to the outer-

most NW3 and SW3, which are just grazed by the slit position (see Fig. 2). Several mechanisms can be proposed to explain these variations in radial velocity and they will be discussed later.

### 3.4. Kinematics of the individual knots

In the following we will analyse in detail the internal kinematics of some of the individual knots. For this we will combine previously existing and new ground-based observations with the high resolution capabilities of STIS.

Fig. 5 shows the emission line profiles derived from STIS data of the  $[\text{N II}]$  6548, 6583 Å, and  $\text{H}\alpha$  6563 Å at the innermost subcondensations SE1a to SE1c and NW1a. The faint subcondensations NW1b and NW1c were barely detected with STIS and consequently are not shown here. The spectra shown are the result of co-adding the signal over the entire spatial extent of each subknot, at slit positions correspondings to the offsets  $-0''.1$ ,  $0''.0$  and  $+0''.1$  with respect to central source (see Fig. 1).

The vertical labels are the relative radial velocities of the high- and low- velocity peaks for the compact subcondensations SE1a, SE1b and SE1c in the receding lobe, and for the knot NW1a in the approaching lobe (Fig. 5).

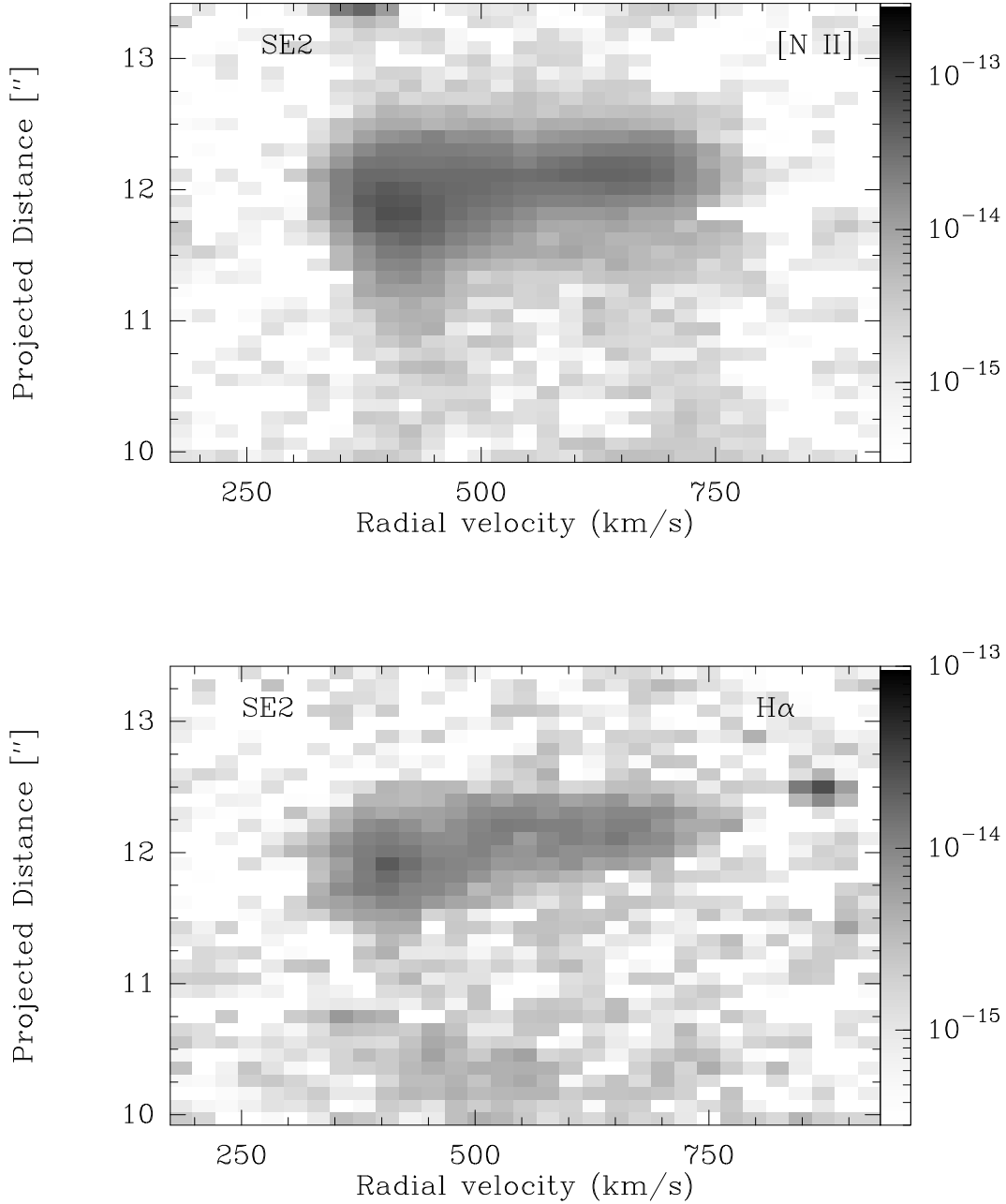


**Fig. 4.** Position-velocity diagram for [N II] 6584 Å (upper panel) and H $\alpha$  6563 Å (lower panel) obtained with STIS (at slit positions +0'2, +0'3, and +0'4 with respect to the central source) through the red-shifted knot SE2. We have used a grey logarithmic scale. The grey bars indicate the flux value in  $\text{erg cm}^{-2} \text{s}^{-1} \text{\AA}^{-1}$ . The ordinate gives the position along the spectrograph slit.

The wide range of velocities covered by each of these compact subcondensations, from 37 to 1093  $\text{km s}^{-1}$  for SE1a, from  $-23$  to 975  $\text{km s}^{-1}$  for SE1b, and from 50 to 865  $\text{km s}^{-1}$  for SE1c, are the largest observed in a PPN. A similar situation is observed in the blueshifted knot NW1a, where all the lines have redward emission extending to  $\simeq 80 \text{ km s}^{-1}$ .

The SE1 subcondensations show double-peaked emission profiles in all the observed emission lines. The strongest peaks are narrower than the weaker and wider low-velocity maxima (see Figs. 5). There is a hint of a

double-peaked profile in SE1a, with the weaker component at approximately 280  $\text{km s}^{-1}$ . The double-peaked profiles are more pronounced in the emission lines formed in SE1b and SE1c.

The condensation NW1a differs from the previously discussed subcondensations in that the low velocity component has slightly stronger intensity than the high velocity component. The emission in NW1a can be seen from about  $-970 \text{ km s}^{-1}$  to  $+80 \text{ km s}^{-1}$  (see Figs. 5). Fig. 3 also shows that the emission extends beyond NW1a. Weak emission is detected at a distance of 3'2 from the central



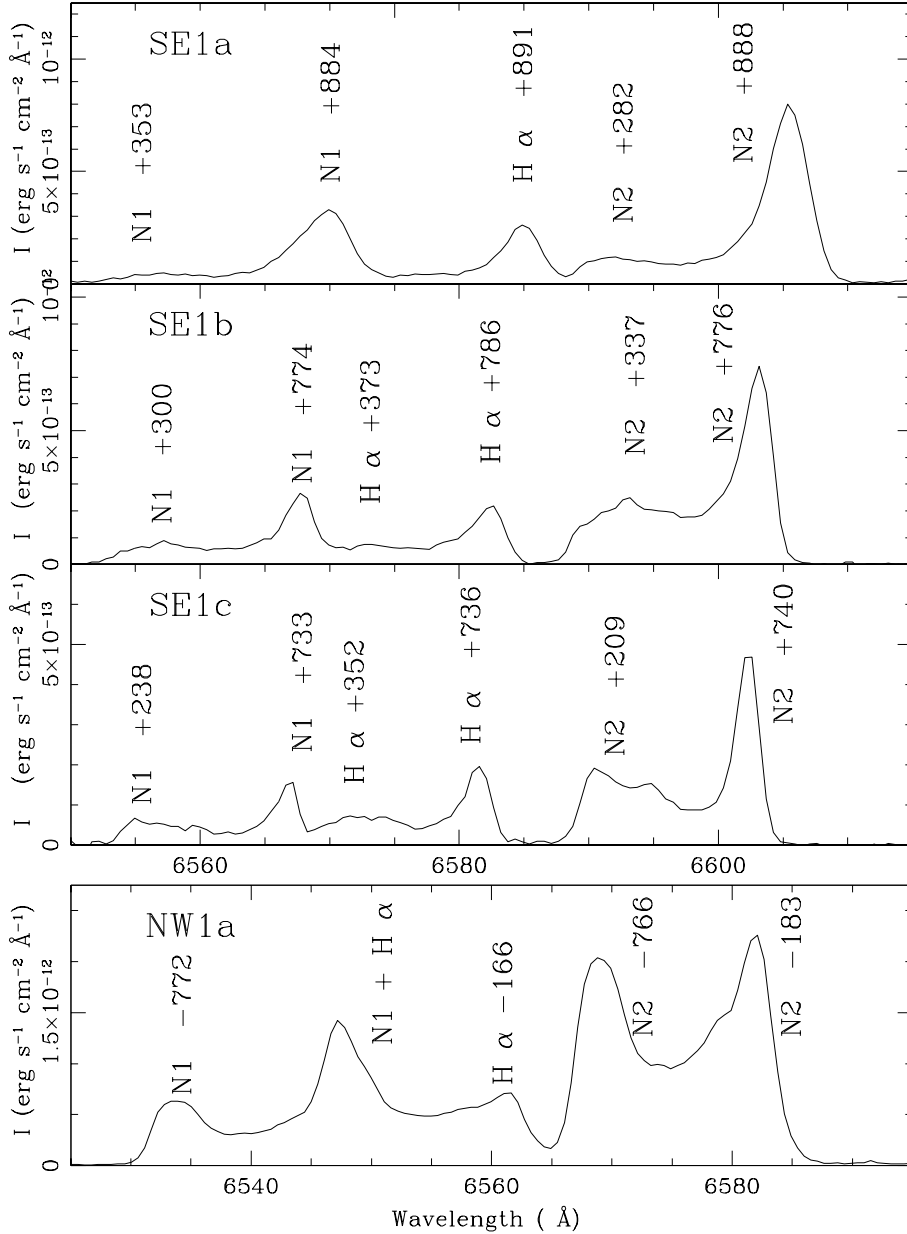


**Fig. 5.** Intensity vs. wavelength profiles of [N II] 6548, 6584 Å, and H $\alpha$  6563 Å for the innermost knots SE1a/b/c and NW1a derived by co-adding the signal over the corresponding angular extent, obtained with STIS at slit positions with offsets  $-0''.1$ ,  $0''.0$  and  $+0''.1$  with respect to the central source. The vertical labels are the relative radial velocity of the peaks. The emission lines are also identified (N1 for [N II] 6548 Å, N2 for [N II] 6583 Å).

core (close to NW1b), with double-peaked emission line profiles at velocities of  $-720$  and  $-230$  km s $^{-1}$  for the high- and low-velocity peaks, respectively.

The intermediate knots (NW2 and SE2) show double-peaked profiles in all lines. A detailed inspection of Fig. 2 shows that the low velocity component of these double-peaked profiles seems to linearly increase its velocity with increasing distance to the center while the high-velocity component (redward in SE2 and blueward in NW2) remains almost constant. The velocity of the low component increases smoothly by 84 km s $^{-1}$  along  $\sim 3''$  in the redshifted lobe, and 77 km s $^{-1}$  in  $\sim 2''$  in the approaching lobe, while the high velocity components remain almost

constant, with fluctuations of just 20 to 30 km s $^{-1}$ . The mean outflow velocity of both knots is  $455 \pm 15$  km s $^{-1}$ , slightly higher than the value of 425 km s $^{-1}$  reported by R95. The emission lines from these knots show extremely large widths of  $\sim 475$  km s $^{-1}$ , slightly larger than the 425 km s $^{-1}$  derived from the emission further away (close to knots NW3 and SE3). It is noteworthy that the low-velocity peaks of NW2 and SE2 knots are stronger in intensity than the high-velocity ones.

Fig. 4 shows the velocity-position contour diagram of the lines H $\alpha$  and [N II] 6584 Å obtained from the STIS spectra of the SE2 knot (see Sect. 2.2.2). We can see that the spectrum displays a highly marked asymmetric shape

with two intensity maxima. This is very similar to the velocity structure usually observed in the spectra of Herbig-Haro (HH, hereafter) objects (Raga 1995).

The STIS spectrum of SE2 also shows that the two maxima are spatially displaced (one with respect to the other). The high-velocity maxima occur  $\sim 0''.15$  farther away from the central star ( $1.3 \times 10^{16}$  cm at a distance of 5.8 kpc). The same was noticed to occur at knot SE1 by BH01, with the lower velocity gas nearer the central star (by  $\sim 0''.05$ ).

Finally, as we have already mentioned, for the first time we have also obtained spectra of the emitting gas of Hen 3–1475 beyond the position of the intermediate knots SE2 and NW2. Our ground-based spectra show that at the outermost regions (i.e. at distances of  $\pm 9''$  from the central source) the emission lines show extremely broad, single-peaked profiles with a mean outflow velocity of  $\pm 405 \pm 15$  km s $^{-1}$  relative to the systemic radial velocity (see Table 1), with a line width (i.e. FWHM) of  $\sim 425$  km s $^{-1}$ .

The mean relative radial velocities of the blueshifted and redshifted peaks derived from our ground-based and STIS spectroscopy are tabulated in Table 1 for these three systems of symmetric knots. The estimated uncertainty for each of these individual velocities is  $\pm 15$  km s $^{-1}$  for ground-based observations, and  $\pm 25$  km s $^{-1}$  for the STIS spectra. The improvement of the S/N ratio of these spectra with respect to previous observations (e.g., R95) allows a more accurate measure of the differences between the low and high velocity emission peaks shown by these knots. These are marked as ‘low’ and ‘high’ in Table 1, which also includes the average velocities and the line widths.

### 3.5. Proper motion measurements and distance

Based on a detailed comparison of the HST WFPC2 images obtained on 1996 June 6 and 1999 September 19 through the F658N filter we have been able to derive for the first time the proper motions of all the system of knots and subcondensations of Hen 3–1475 above described. BH01 reported proper motion measurements only for the intermediate knots, since their main interest was just the determination of the distance towards Hen 3–1475. We have extended the analysis to all the emitting knots in Hen 3–1475 because this can provide us relevant information on the physical process(es) responsible for the formation of these structures.

In order to carry out these proper motion measurements, the first- and second-epoch F658N images were converted into a common reference system, with the Hen 3–1475 jet along the  $y$  axis, oriented at a P.A. of  $136^\circ$ . After the transformation, the average and r.m.s. of the difference in position for eight reference stars in the field appearing in two images was  $-0.318 \pm 0.080$  pixels (equivalent to  $-0''.0145 \pm 0''.0036$ ) in the  $x$  coordinate and  $0.050 \pm 0.060$  pixels (equivalent to  $0''.0031 \pm 0''.0027$ ) in the  $y$  coordinate.

After this, we computed the two-dimensional cross-correlation function of the emission detected within small, previously defined boxes containing the individual condensations under study. Finally, the proper motions were determined through a parabolic fit to the peak of the cross-correlation function (see Reipurth et al. 1992 and López et al. 1996 for a detailed description of this method). The uncertainty in the position of the correlation peak derived this way was estimated through the scatter of the correlation peak positions obtained from boxes differing from the nominal one in 0 or  $\pm 2$  pixels ( $0''.090$ ) in any of its four sides, making a total of  $3^4 = 81$  different boxes for each knot. The error adopted has been twice the r.m.s. deviation of the position found, for each coordinate, added quadratically to the r.m.s. alignment error. The numerical results obtained for the system of knots in Hen 3–1475 are shown in Table 2, which includes the derived proper motions (in milliarcsec yr $^{-1}$ ), the tangential velocities (in km s $^{-1}$ ) for an adopted distance of 5.8 kpc (see below), as well as the position angle of the proper motion vectors (in degrees).

In Fig. 6 we show the F658N HST 1999 image of Hen 3–1475, with each knot identified with a label. The arrows indicate the proper motion velocity vector associated with each knot derived with this method, and the ellipses at the end of each arrow indicate the uncertainty.

In order to perform an accurate determination of the distance to Hen 3–1475, it is appropriate to base it on the proper motions of the intermediate knots, which most likely correspond to internal working surfaces (see Sect. 4), and whose radial velocities and proper motions should provide a good measure of the actual space velocity of the knots (Raga et al. 1990).

We find remarkably similar proper motions for the NW2 and SE2 knots, with an average value of 13.2 milliarcsec yr $^{-1}$ , somewhat larger than the results obtained by BH01. Combining the radial velocity of 455 km s $^{-1}$  associated to with these knots (see Sect. 3.4) with an inclination angle of the axis of  $50^\circ \pm 5^\circ$  with respect to the plane of the sky (BH01), we find the distance to Hen 3–1475 to be 5.8 kpc (for  $i = 45^\circ$  and  $55^\circ$  the distances would be 6.9 and 4.9 kpc, respectively), significantly smaller than the value of  $8 \pm 2$  kpc derived by BH01. BH01 adopt a larger radial velocity and a lower proper motion for the intermediate knots resulting in a larger distance.

In the NW lobe, tangential velocities range from 100 to 365 km s $^{-1}$  (for an adopted distance of 5.8 kpc). The knots in this lobe move along the jet axis at an average position angle of  $302^\circ$ . We find remarkably similar tangential velocities ( $\sim 350$  km s $^{-1}$ ) and large proper motions for the knots NW2 and NW3 while the subcondensation NW1a shows a smaller tangential velocity ( $\sim 200$  km s $^{-1}$ ) and proper motion in the direction of the jet axis. Even smaller tangential velocities and proper motions are detected (just at  $\sim 2\sigma$  level) in the subcondensations NW1b and NW1c, although they still seem to follow very closely the axis of the jet.

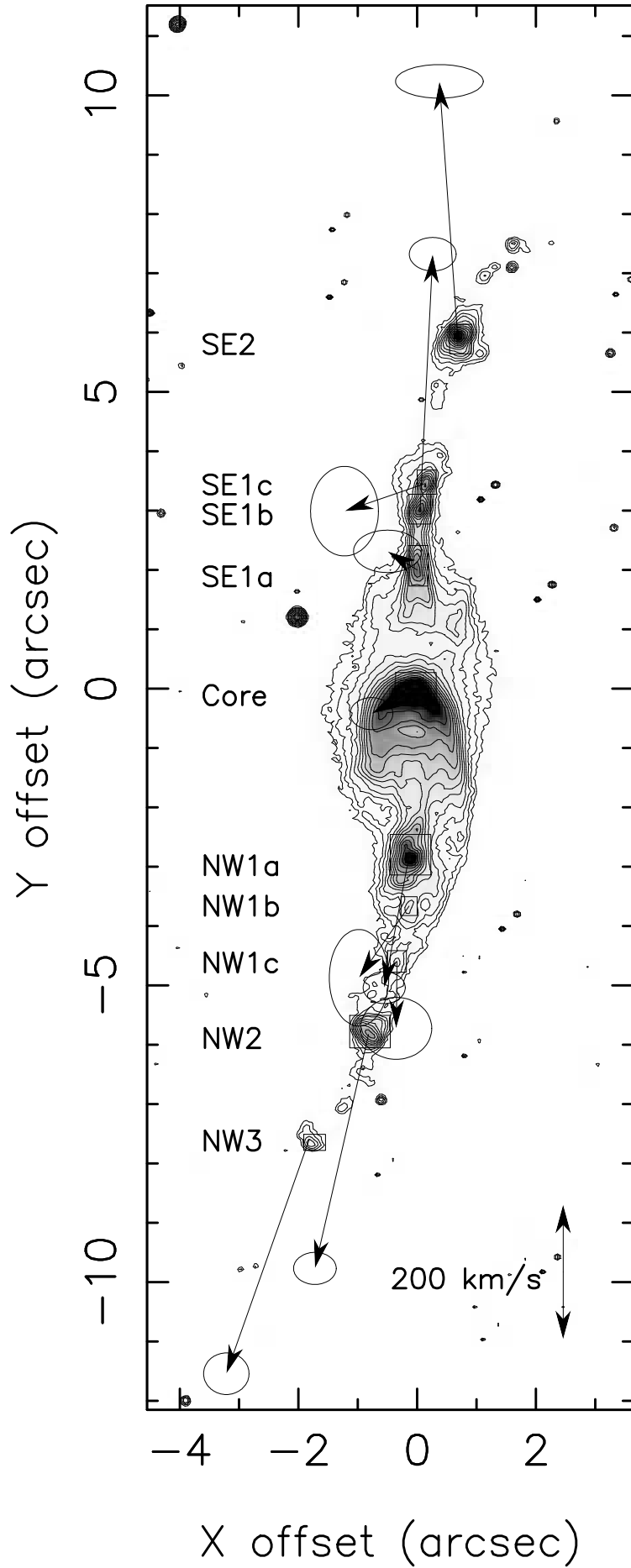


Fig. 6. HST I-band image of Hen 3–1475 overlaid with the  $\text{Fe}50\text{N}(\text{Cl})$  derived from the 1000 km/s  $\text{Fe}50\text{N}(\text{Cl})$  emission line. The contours are overlaid on the image. The arrows indicate the outflow direction. The scale bar represents 200 km/s.

**Table 1.** Relative radial velocities of [NII] 6584 Å

Region	Observations	High (km s <sup>-1</sup> )	Low (km s <sup>-1</sup> )	Average (km s <sup>-1</sup> )	Line width (km s <sup>-1</sup> )
NW1a	HST + STIS	-766	-183	-475	1050
SE1a	HST + STIS	+888	+282	+585	1056
SE1b	HST + STIS	+776	+337	+556	998
SE1c	HST + STIS	+740	-	-	815
NW2	INT + IDS	-552	-367	-460	475
SE2	INT + IDS	+540	+355	+447	475
NW3	INT + IDS	-	-	-403	425
SE3	INT + IDS	-	-	+405	425

**Table 2.** Proper motion measurements and tangential velocities in Hen 3–1475

Knot	$\mu_x$ (milliarcsec yr <sup>-1</sup> )	$\mu_y$ (milliarcsec yr <sup>-1</sup> )	Tangential velocity (km s <sup>-1</sup> )	P.A. (°)
SE2	-0.99 ± 4.70	+13.80 ± 0.90	377	140
SE1c	-4.35 ± 4.82	-1.49 ± 2.41	125	245
SE1b	+0.69 ± 4.60	+13.80 ± 0.90	376	133
SE1a	-1.60 ± 4.82	+1.00 ± 1.14	51	194
NW1a	-1.34 ± 4.56	-7.08 ± 0.86	196	305
NW1b	-2.70 ± 4.83	-3.86 ± 2.60	128	281
NW1c	-0.04 ± 4.96	-3.60 ± 1.67	98	315
NW2	-2.89 ± 4.73	-12.60 ± 0.86	353	312
NW3	-4.46 ± 4.73	-12.60 ± 1.12	365	297

In the SE lobe both the knot SE2 and the inner subcondensation SE1b show a remarkably similar tangential velocity (376 km s<sup>-1</sup>) and proper motion along the axis of the jet (with an average position angle of 136°). However, the innermost knots SE1a and SE1c do not show any significant proper motion within the errors. The measurements may be affected by the variation with time of their shapes, as suggested by the completely different direction of motion shown by these subcondensations. Unfortunately, we could not determine the proper motion of knot SE3 since this knot was affected by a bad CCD column in one of the images.

Using the proper motions derived above for the knots and their angular distances to the central source, we can estimate kinematic ages for the individual knots. The position of NW2 and SE2 (quoted in Table 3) together with the derived proper motion of 12.6 and 13.8 milliarcsec yr<sup>-1</sup>, respectively, lead to a kinematic age of ~ 450 years for the intermediate knots. A similar procedure applied to the outermost knots NW3 and SE3, adopting for both the proper motion of 12.6 milliarcsec yr<sup>-1</sup> measured for NW3, gives a kinematic age of ~ 600 years. The kinematic ages of the intermediate and outermost knots (with an age difference of  $\simeq$  150 years between both system of knots) is compatible with the evolutionary stage of the central star and with the variable velocity model outlined below (see Sect. 4.3.3).

**Table 3.** An estimation of the kinematic ages of the intermediate and outer pairs of knots observed in Hen 3–1475

Knot	Angular distance (arcsec)	Tangential velocity (km s <sup>-1</sup> )	Dynamical ages (years)
NW2	5.83	353	463
SE2	5.92	377	429
NW3	7.82	365	620
SE3	7.57	365*	601

\* assumed value

## 4. Discussion

### 4.1. Line excitation mechanism

The emission observed in the intermediate knots of Hen 3–1475 was found to be formed in the recombination region of shock waves (R95). The spectra of NW2 and SE2 are characterized by extremely large [N II]/H $\alpha$  ratios (~ 3.0), and electron densities of ~ 3000 cm<sup>-3</sup>. R95 qualitatively determined the shock velocity needed to reproduce the observed [O III]/H $\beta$  and [O I]/H $\alpha$  ratios by comparison with plane-parallel shock models from Hartigan et al. (1987), which adopt solar abundances in their calculations. The ratios observed in the middle knots were compatible with intermediate shock velocities of ~ 100 km s<sup>-1</sup>.

In order to estimate the N/H relative abundance R95 compared the [N II]/H $\alpha$  ratios with the planar shock models (for a shock velocity of 100 km s<sup>-1</sup>) computed by Dopita et al. (1984a), and derived a N/H abundance of

$(3.6 \pm 0.6) \times 10^{-4}$  assuming a linear dependence between the  $[\text{N II}]/\text{H}\alpha$  ratio and the  $\text{N}/\text{H}$  relative abundance.

We can also determine the shock velocities able to reproduce the observed optical spectra by relaxing the *a priori* assumptions on the shock velocity and fixing instead the gas abundances. None of the predictions of plane-parallel shock models for different shock velocities in the literature (e.g. Shull & McKee 1979; Dopita et al. 1984a; Hartigan et al. 1987) can reproduce the  $[\text{N II}] 6548, 6583 \text{ \AA}/\text{H}\alpha$  and  $[\text{N I}] 5200 \text{ \AA}/\text{H}\beta$  emission line ratios observed in Hen 3–1475. Neither the bow-shock models available to now can predict the observed line ratios (Hartigan et al. 1987). None of these models are applicable to PNe abundances, except the plane-parallel shock model computed by Meaburn et al. (1988) to reproduce the spectra of the outer shell of  $\eta$  Carinae, which shows very high  $[\text{N II}] 6583 \text{ \AA}/\text{H}\alpha$  emission line ratios ( $\sim 2.8$ ). Meaburn et al. (1988) assumed a  $\text{N}/\text{H}$  relative abundance of  $10^{-3}$  and a shock velocity of  $140 \text{ km s}^{-1}$ . Since none of the available grids of plane-parallel or bow-shock models are applicable to PNe, we have obtained a grid of (steady 1-D) plane-parallel shock models with the photoionization-shock code MAPPINGS Ic (Binette et al. 1985; Dopita et al. 1984b) adopting the mean Type I PNe abundances which are characterized by their high  $\text{N}/\text{O}$  abundance ratio (Kingsburgh & Barlow 1994), and a pre-ionized gas with  $n_{\text{H}} = 50 \text{ cm}^{-3}$  (which fits the observed electron densities derived from the  $[\text{S II}]$  doublet lines). By comparing the observed emission line ratios for the intermediate knots (Table 4 of R95) with our predictions of planar shock models, we can determine the velocity of the shocks responsible for the observed spectra.

The results are shown in Fig. 7, where the observed and predicted emission line ratios are plotted for comparison. Fig. 7 illustrates that the observed  $[\text{N II}] 6584/\text{H}\alpha$  ratios are reasonably well reproduced for a wide range of shock velocities (from  $100$  to  $250 \text{ km s}^{-1}$ ), while the values of the temperature-dependent ratio  $[\text{N II}] (6584 + 6548)/5755$  are only marginally reproduced for a shock velocity  $\sim 100 \text{ km s}^{-1}$  (other models predict higher values which means lower  $T[\text{N II}]$ ). The  $[\text{N I}] 5200/\text{H}\alpha$  ratios are reproduced for shock velocities from  $100$  to  $150 \text{ km s}^{-1}$ . These results confirm that the gas is nitrogen enriched.

In addition, the observed  $[\text{O III}] 5007/\text{H}\alpha$  ratios are reproduced only for shock velocities higher than  $120 \text{ km s}^{-1}$  (at least the observed value in the SE2 knot).

However, the models predict too low  $[\text{O I}] 6300/\text{H}\alpha$  and slightly low  $[\text{S II}] (6717+6731)/\text{H}\alpha$  ratios. The weakness of the  $[\text{O I}]$  and  $[\text{S II}]$  emission lines predicted by the shock models, leading to a disparity between the observed and predicted emission line intensities, is not surprising since shock models appear to have problems in reproducing the observed  $[\text{O I}]/\text{H}\alpha$  and  $[\text{S II}]/\text{H}\alpha$  line ratios in SN remnants and HH objects too (see, e.g., Dopita et al. 1984b; Raga et al. 1996).

A clear problem is that we are comparing the emission line ratios from the knots NW2 and SE2, which are curved structures, with plane-parallel steady models. In a curved

shock we expect contribution from the more oblique, lower shock velocity regions, and from higher shock velocity regions. The geometry of the condensation also influences on the ionization of the pre-shock gas, which strongly determines the post-shock emission. On the other hand, the plane-parallel models presented here do not include magnetic fields. We assume that the strength of the magnetic field is small at the location of the intermediate knots. If magnetic fields ( $\sim 0.1$  to  $30 \mu\text{G}$ ) are included the compression in the recombination region is reduced (Shull & McKee 1979, Morse et al. 1992). The effect on the observed spectra is a reduction of the  $[\text{O I}]$  and  $[\text{N I}]$  intensities (Shull & McKee 1979, Morse et al. 1992, Morse et al. 1993). If the magnetic fields are strong we might be underestimating the shock velocity (as pointed out by Trammell & Goodrich 2002).

In summary, the attempt to model the observed emission line ratios in Hen 3–1475 using plane parallel shocks can be considered as partially successful. The results are in most cases consistent with a spectrum arising from the recombination region of a shock wave with shock velocities ranging from  $100$  to  $150 \text{ km s}^{-1}$ , moving through a nitrogen enriched gas.

## 4.2. Analysis of the emission line profiles

In the following we will try to describe the main properties of the line profiles observed in order to set constraints on the physical mechanisms responsible for this emission.

Some of the properties of the emission knots in Hen 3–1475 have been observed before in at least some well-known HH objects. They show also prominent double-peaked profiles and extraordinarily large line width. For instance, the HH 32 objects show line widths exceeding  $350 \text{ km s}^{-1}$  (Solf et al. 1986; Hartigan et al. 1986a); the HH objects in Cepheus A show large line widths  $\sim 475 \text{ km s}^{-1}$  (Hartigan et al. 1986b), while the most extreme radial velocities are observed in HH 80-A and HH 81-A, with a line width of  $700 \text{ km s}^{-1}$  (Heathcote et al. 1998).

Usually, the low-velocity component of the double-peaked emission line profiles observed in these HH objects is stronger than the high-velocity component, as is also observed in the intermediate knots of Hen 3–1475. The reversed situation, which is found at the innermost subcondensations of SE1, has also been found in a few HH objects, as HH 32D (Solf et al. 1986; Hartigan et al. 1986a).

HH objects showing wide double-peaked emission line profiles have been explained in terms of bow-shock models (e.g. Raga & Böhm 1986; Hartigan et al. 1987). The bow-shock contains a large range of velocities projected along the line of sight that explain how a small volume can produce wide emission line profiles. Under certain inclination angles (for oblique viewing angles), the bow-shock models predict the existence of two maxima with the low-velocity maximum being brighter than the high-velocity peak (“in-

terstellar bullet” or bow-shock facing away from the central source) or with the high-velocity component stronger than the low-velocity emission peak (“stationary shocked cloudlet” or bow-shock facing towards the central source).

The intermediate knots SE2 and NW2 in Hen 3–1475 share some of the properties mentioned above for “facing away bow-shocks”: extremely wide emission line profiles with the presence of two peaks, where the low-velocity component shows a higher intensity, and both knots show high proper motions. The inclination angles, with respect to the plane of sky, required to reproduce the observed double-peaked profiles (which have to be  $\geq 45^\circ$ ; Raga & Böhm 1986; Hartigan et al. 1987) are compatible with the adopted inclination angle of  $50^\circ \pm 5^\circ$  for Hen 3–1475. There are, however, some difficulties with the simple bow-shock model. The spatial velocity displacements of the low and high radial velocity gas found in the 2-D spectra of Hen 3–1475 and the increase of the radial velocity of the low-velocity gas in NW2 and SE2 with distance to the source contradict the predictions of 2-D bow-shock models (Raga & Böhm 1986). We should note that the details of the density structure in the shock has a strong effect on the shapes of the emission-line profiles, even with simple geometries. Bobrowsky & Zipoy (1989) show a variety of line profiles arising from different density distributions along the line of sight.

In addition, the intermediate knots of Hen 3-1475 show high tangential velocities comparable to the tangential velocities observed in several HH objects (see, e.g., Eislöfel et al. 1994), and in agreement with predictions of the variable ejection velocity models (see below). The complex structure and kinematics of the innermost knots remain intriguing. These knots show extremely large line widths ( $\sim 1000 \text{ km s}^{-1}$ , see Table 1) which imply a complex kinematics on subarcsecond scales. The situation is apparently more difficult to explain considering that subcondensations NW1a and SE1b appear to move with high tangential velocities while subcondensations SE1b and SE1c, and possibly NW1b and NW1c, appear to be stationary.

#### 4.3. Kinematics of the outflow

BH01 interpreted the emission line profiles of the knots as well as the decrease of the radial velocity with distance to the source as signatures of violent deceleration of the outflow both at small (a few  $10^{16}$  cm) and large (along the axis within a few  $10^{17}$  cm) scales as the result of turbulent interaction between the jet and the surrounding ambient gas.

However, as we will see below, the strong deceleration claimed to occur at small scales within individual knots by BH01 (up to  $\sim 600 \text{ km s}^{-1}$  in distances of the order of  $\sim 10^{16}$  cm) cannot occur for realistic values of the relevant parameters in Hen 3–1475. In addition, at large scales, there are other mechanisms, apart from the interaction of the jet with the surrounding ambient gas proposed by BH01, which cannot be discarded as responsible for

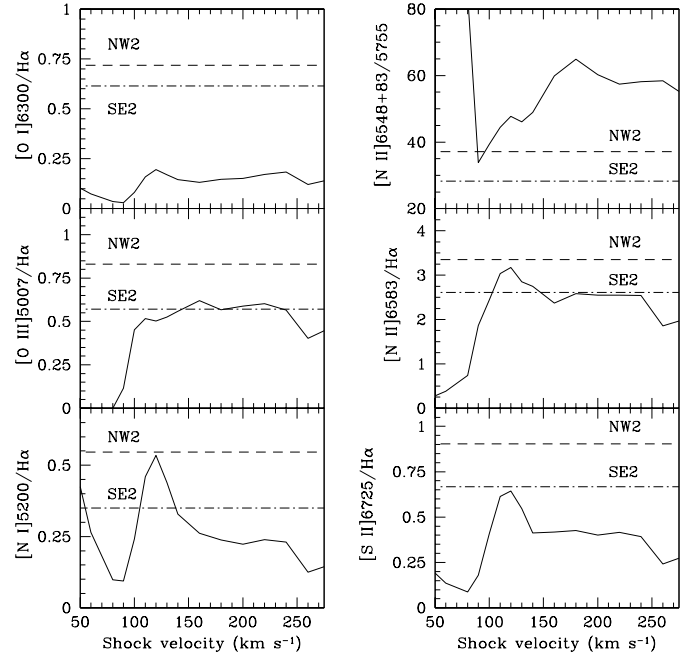


**Fig. 7.** Predicted emission line ratios for a grid of 1-D steady shock models as a function of shock velocity (solid line). Dashed lines are the observed emission line ratios for NW2 (dashed line) and SE2 (dot-dashed line) (from R95).

the observed decrease of the radial velocity, such as geometrical effects (due to precession) and/or to variability of the ejection velocity (consequence of a variable, may be episodic, stellar wind), which are briefly discussed below.

##### 4.3.1. A geometrical effect induced by precession

At first sight, the lack of alignment between the different knots seems to favour the possibility that the direction of ejection could actually be varying with time. In order to reproduce the observed S-shaped morphology of Hen 3–1475 in terms of precession, this motion would require an aperture angle  $< 10^\circ$ , and a period  $\sim 1500$  years. However, such a precession, considered alone, cannot reproduce the whole system of radial velocities observed (see R95 for a more detailed discussion).

##### 4.3.2. Interaction with the ambient medium

Two possibilities exist under this scenario. Either the deceleration of the jet along its axis occur in a turbulent jet beam which incorporates matter through a sideways entrainment process, or this deceleration is the result of the interaction of a fragmented jet with the external medium.

In order to explore the first of the two possibilities, De Gouveia dal Pino (2001) simulated a 3-D pulsed HH jet, illustrating that deceleration of the internal working surfaces (identified with the knots) occurs when moving away from the central source as momentum is transferred by the gas expelled sideways from the traveling pulses.

These simulations predict a slow-rate decrease of the speed of the internal working surfaces, with a final drop of the velocity at the position of the leading working surface. The smooth fall off of the velocity of the internal working surfaces with distance (velocities decrease by  $\sim 20 \text{ km s}^{-1}$  along  $5 \times 10^{17} \text{ cm}$  for an initial ejection velocity of  $\sim 100 \text{ km s}^{-1}$ ) obtained by De Gouveia dal Pino (2001) do not fit the step-like decrease of the radial velocity with increasing distance and the abrupt velocity variation at the position of the intermediate knots shown by Hen 3–1475.

This entrainment process could actually contribute to the decrease of the velocity of the internal working surfaces as they travel away from the central source, but cannot be responsible for the bulk of the slowing down observed along the jet of Hen 3–1475. A numerical simulation with the actual values (velocity, density, and time-scale variability) applicable for Hen 3–1475 would be needed to quantify the exact contribution to the general slowing down observed along the jet that could be due to this effect.

The second possibility is that the observed deceleration could be the result of drag forces of the ambient medium on individual jet knots, as suggested by Cabrit & Raga (2000) to explain the jet deceleration in HH 34. This scenario is compatible with the fragmentation into a series of clumps of a jet with a periodic velocity variability and a slow precession (Raga & Biro 1993), which is likely to be the case of Hen 3–1475.

We explore this situation, in which the jet fragments produce “interstellar bullets” which are slowed down by the interaction with the surrounding material (i.e. the AGB remnant) using the analytical approach of Cabrit & Raga (2000).

For this calculation we will choose a value of the isothermal sound speed of  $10 \text{ km s}^{-1}$ . In addition, we need to estimate the mass of the clumps and the environmental density, which are not well known. If we consider a pre-shock density of  $n_{\text{H}} = 50 \text{ cm}^{-3}$  (see Sect. 4.1) and a size of a few  $10^{16} \text{ cm}$  for the intermediate knots (adopting a distance of 5.8 kpc and a filling factor  $\sim 1$ ), we can infer a mass for these knots of  $\sim 10^{-5} M_{\odot}$ .

With respect to the environmental density, we have to consider the presence of the molecular torus around the central source detected in CO (Knapp et al. 1995; Bujarrabal et al. 2001) and OH (Bobrowsky et al. 1995; Zijlstra et al. 2001) which indicates the existence of an equatorial density enhancement in the AGB ejecta.

Adopting the mass loss rate and the polar dependence of the AGB wind from Mellema (1995), a value  $\leq 300 \text{ cm}^{-3}$  at a distance of  $2.5 \times 10^{17} \text{ cm}$  from the central star is inferred for the density of the environmental material that would interact with the highly collimated gas ejected along the poles (for a ratio between the density at the equator and at the poles of 5.0 and assuming that the environmental density decreases with distance as  $r^{-2}$ ). The deceleration curve (position versus velocity) derived is shown as a solid line in Fig. 8 for an initial velocity of  $1200 \text{ km s}^{-1}$ . We can see that the predicted decrease of

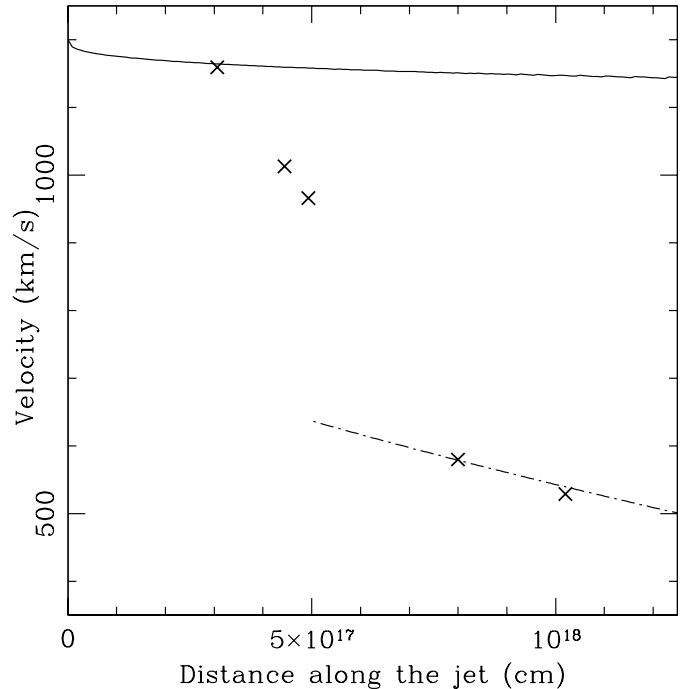


**Fig. 8.** Predicted deceleration curves (position-velocity) for constant mass knots decelerated by the ambient medium (see Sect. 4.3.2). The values of the observed velocity and distance to the source of the innermost and intermediate knots are shown as crosses.

the radial velocity with distance to the source due to the drag force cannot explain by itself the strong deceleration observed in the innermost regions of the outflow, nor the difference in velocity observed between the internal knots and the intermediate ones. However, it can perfectly explain the observed deceleration from SE2 to SE3 (dotted line of Fig. 8) for an initial velocity of  $\sim 775 \text{ km s}^{-1}$  and a density of  $\sim 50 \text{ cm}^{-3}$  at the location of the intermediate knots.

Our conclusion is that only the small deceleration occurring at large scales (slowing down of the velocity of the knots of  $\sim 50 \text{ km s}^{-1}$  along few  $10^{17} \text{ cm}$ ) from the intermediate knots to the outermost knots of Hen 3–1475 can be explained as the result of drag forces of the ambient medium and/or entrainment as the knots move outwards, while the strong deceleration claimed to occur at smaller scales by BH01 (with deceleration of  $\sim 600 \text{ km s}^{-1}$  along few  $10^{16} \text{ cm}$ ) are unlikely to be caused by this environmental drag.

#### 4.3.3. A changing stellar wind with variable ejection velocity

The step-like velocity variations observed in the innermost subcondensations very close to the central source in Hen 3–1475 invite to suggest the possibility of interpreting these knots as bow-shocks formed in the outflow as a consequence of a changing stellar wind with a variable velocity ejection (perhaps episodic mass loss events).

Different physical scenarios might form bow-shocks. In the “shocked cloude” model the HH knots are slowly moving condensations, embedded in a supersonic wind ejected from the exciting source (Schwartz 1978). Bow-shocks directed away from the central star can be formed by the interaction of clumps of gas with the ambient medium during discrete events of ejection (scenario known as the “interstellar bullet” model which was introduced by Norman & Silk (1979)). More recent models are based on the idea that HH emission is associated with shocks produced in jet-like outflows. Bow shock-like structures (identified with the knots) can be formed in a jet-like outflow as a result of a variability of the ejection velocity (see Raga 1991 for a detailed description of the origin of the bow-shock like structures within HH jets; Hartigan & Raymond 1993; Stone & Norman 1993a,b; De Gouveia Dal Pino & Benz 1993, 1994). It has been shown that for a quasi-periodic velocity variability with a highly supersonic velocity amplitude, shocks develop in the beam which are arranged in two-shock structures called ‘internal working surfaces’ which are identified with the knots (see, e.g., Raga et al. 1990; Hartigan and Raymond 1993).

Raga & Biro (1993) showed — analytically and numerically — that a jet with a quasi-periodic variability and a slow precession would fragment into clumps which behave like the “interstellar bullets” proposed by Norman & Silk (1979). Such a variability might be responsible for the formation of the knots of the jet in Hen 3–1475, since its point-symmetric morphology suggests that the direction of ejection is actually varying as a function of time. The predictions of this model are compatible with the high proper motions measured for the knots, the presence of the double-peaked wide emission line profiles, the relative intensities of the high and low-velocity components (at least in the intermediate knots) and the shock velocities derived in Hen 3–1475.

Detailed numerical models able to predict the kinematics and emission line ratios along jets of this kind are needed to check whether other properties shown by Hen 3–1475 could also be explained in this scenario. The extreme properties shown by the innermost knots and the lack of proper motions in their subcondensations, for instance, are difficult to reproduce with the simple model outlined above.

To investigate whether a variation in the ejection velocity could induce the formation of the knots observed in Hen 3–1475 we can carry out a comparison of some observed properties with the predictions of the analytical 1-D model by Raga et al. (1990). The 1-D analytical approximation for prepressure-matched jets predicts that the emission observed in the internal working surfaces would mainly come from shocks of velocity  $V_s \simeq 1/2(u_1 - u_2)$ , and the internal working surface should be moving at  $V_{ws} \simeq 1/2(u_1 + u_2)$ , where  $u_1$  and  $u_2$  are the velocity of the flow before and after the jump associated with the knots (Raga et al. 1990). From the data shown in Table 1 for SE2 and NW2, we deduce shock velocities of  $200 \text{ km s}^{-1}$ , and tangential velocities for the internal working surfaces

of  $475 \text{ km s}^{-1}$  (for an inclination angle of  $50^\circ$ ). The predicted  $V_s$  is in qualitative agreement with the observed spectra, and the observed tangential velocities of NW2 and SE2 ( $\sim 400 \text{ km s}^{-1}$ ) are also comparable to the predicted value of  $475 \text{ km s}^{-1}$ . It is interesting to notice the good agreement between the predicted and observed values of the shock velocity and the velocity of the intermediate knots from a simple 1-D model for a constant density jet.

For a highly supersonic flow (i.e. in the absence of prepressure forces), the fluid parcels move ballistically, and for the asymptotic regime of large distances from the central source, all the internal working surfaces should move with the same velocity  $V_{ws}$  (see Sect. 3.4 of Raga & Kofman 1992). The variability period can then be calculated by combining this velocity  $V_{ws}$  with the spatial separation between two successive knots (Raga & Kofman 1992). The intermediate and outermost knots of the blueshifted side of the jet move with similar velocities as required above (see Table 3). From the spatial distance between the intermediate and outermost knots ( $d_{ws}$  taken from Table 3) we estimate a timescale  $\tau \simeq d_{ws}/V_{ws} \simeq 100$  years for the variability of the velocity of the jet.

It is interesting to note that variability over periods of few hundred years have been found to occur in some PPNe and PNe, through the detection of concentric circumstellar arcs and rings, viewed in scattered light (see Hrivnak et al. 2001 and references therein). The arcs are interpreted as the result of quasi-periodic mass-loss events of very short duration experienced by the central star.

The physical origin of these short periods of enhanced mass loss is still unknown. The associated timescales are much longer than the observed pulsational periods of AGB stars (300 to 1000 days, typically), but much shorter than the timescale of thermal pulses ( $10^4$ – $10^5$  years).

Several mechanisms have been proposed:

- instabilities in the gas-dust coupling in a radiation pressure-driven outflow that can create density waves that appear as discrete shells (Deguchi 1977),
- the possible influence of the presence of a binary companion, creating cyclical perturbations in the mass outflow (Harpaz et al. 1997; Mastrodemos & Morris 1997),
- a magnetic cycle leading to coronal ejection-like events as a consequence of the dynamo action induced by the differential rotation between the rapidly rotating stellar core and the more slowly rotating envelope of the star (Soker 2000; Blackman et al. 2001a).

On the other hand, the apparent slowing down of the jet of Hen 3–1475 (from  $\sim 1200 \text{ km s}^{-1}$  at the innermost knots to  $\sim 600 \text{ km s}^{-1}$  at the intermediate knots) would indicate that, superimposed on the quasi-periodic velocity variability giving rise to the internal working surfaces (e.g. the knots), there is an underlying trend of increasing ejection velocity over time (as was first proposed by R95).



#### 4.4. Nature and evolutionary stage of Hen 3–1475

At a distance of 5.8 kpc the stellar luminosity of the central source of Hen 3–1475 is  $\sim 12600L_{\odot}$ , typical of a relatively high luminosity post-AGB star, but half the value derived by BH01, confirming the results of R95.

The mass loss rate can be estimated in the following way. If we idealize the flow as a cylinder of radius  $R$ , with gas of uniform density  $\rho$  that moves at a velocity  $V$ , then  $\dot{M} \simeq \pi R^2 \rho V$ . For the observed parameters at the position of the intermediate knots, with  $R \simeq 3 \times 10^{16}$  cm, a pre-shock density  $\sim 50 \text{ cm}^{-3}$  and a velocity of  $600 \text{ km s}^{-1}$  (adopting an inclination of  $50^\circ$ ), we derive a mass loss rate  $\dot{M} \sim 2 \times 10^{-7} M_{\odot} \text{ yr}^{-1}$ ; also compatible with the star being in the post-AGB phase.

Therefore, the wind kinetic luminosity and kinetic momentum are  $L \simeq \dot{M} V^2 \simeq 6 \times 10^{34} \text{ erg s}^{-1}$  and  $P \simeq \dot{M} V \tau \simeq 10^{37} \text{ g cm s}^{-1}$  (adopting a kinetic age  $\tau \simeq 600$  years), respectively. From the above data, we can also estimate the total kinetic energy of the high-velocity outflow, which is  $\simeq 10^{45} \text{ erg}$ .

Different models for the formation of highly-collimated jets in post-AGB stars have been proposed. Magnetohydrodynamical models can form collimated structures from a single rotating star (García-Segura et al. 1999), while other theories require the presence of an accretion disk (Soker & Livio 1994; Blackman et al. 2001b). Images of the young PN He 3–1357 show collimation of outflows by an outer, previously ejected gas shell (Bobrowsky et al. 1998).

3-D MHD simulations by García-Segura & López (2000) showed that jets form as a result of the action of the hoop stress caused by the toroidal magnetic field; these jets can be detected if the mass loss rate of the fast wind is  $\geq 10^{-7} M_{\odot} \text{ yr}^{-1}$ , which is the case of Hen 3–1475.

In the numerical simulations by García-Segura et al. (1999) and García-Segura & López (2000), jets form at distances of  $\sim 10^{17}$  cm from the central star. We should note that in the simulations by García-Segura & López the fast wind velocities are  $\sim 100 \text{ km s}^{-1}$ , which is significantly slower than the wind velocity observed in Hen 3–1475 (R95; Sánchez Contreras & Sahai 2001). The increase of the fast wind velocity in the MHD simulations of García-Segura et al. does not prevent the formation of the highly collimated structures. The only difference is that for higher wind velocities the collimation of the jet occurs at even larger distances from the central source (i.e.  $> 10^{17}$  cm). This is more than the distance at which collimation is present in Hen 3–1475 (at  $\sim 10^{16}$  cm; Sánchez Contreras & Sahai 2001). Otherwise, the mass loss rate and/or the magnetic fields should be increased for the collimation to occur at shorter distances from the central source.

In the MHD models, point symmetric morphology may be caused by precession or may result from a steady misalignment of the magnetized wind axis with respect to the axis of the bipolar wind outflow (García-Segura 1997, García-Segura & López 2000). Both cases require the existence of a binary companion.

In order to explain the presence of episodic ejection (or quasi-periodic variability) MHD instabilities in a magnetized outflow are invoked. The 3-D MHD simulations by García-Segura (1997) show that the collimated outflow is likely to be subject to kink instabilities, which can lead to the formation of blobs resembling the knots of a jet. Otherwise, the formation of an episodic jet can be produced by periodic variations of the magnetic field, as the cyclic polarity inversion of the magnetic field introduced by García-Segura et al. (2001) to reproduce the concentric rings observed in many PPNe and PNe.

Another mechanism that might be responsible for the formation of the jet of Hen 3–1475 is the presence of an accretion disk (Soker and Livio 1994; Blackman et al. 2001b). The formation of an accretion disk in PNe requires the existence of a binary companion (Soker 1998; Soker & Livio 1994; Reyes-Ruiz & López 1999).

The expected properties of a jet driven by an accretion disk formed at the end of the common-envelope phase deduced by Soker & Livio (1994) (mass loss rate into the jet  $\sim 10^{-7} M_{\odot} \text{ yr}^{-1}$  to  $10^{-6} M_{\odot} \text{ yr}^{-1}$ , and jet velocities  $\sim 500 \text{ km s}^{-1}$ ) qualitatively agree with the properties of the jet observed in Hen 3–1475.

Recently, Blackman et al. (2001b) present a MHD model to describe the interplay between disk winds and stellar winds in the context of PPNe, where both the star and the accretion disk may blow outflows. For ages of a few hundred years, disk winds — which dominates over the stellar wind — can supply  $\sim 2 \times 10^{34} \text{ erg s}^{-1}$ , which is compatible with the estimated kinetic luminosity ( $\sim 6 \times 10^{34} \text{ erg s}^{-1}$ ) and the estimated age ( $\sim 600$  years) of Hen 3–1475.

If the outflow is due to the magneto-hydrodynamical collimation of the disk (or disk + star) wind, precession could be radiation-induced by the irradiation of the disk by the central source (Livio & Pringle 1997). As the disk wobbles, there are episodes of an enhanced accretion rate with timescales  $\leq 1000$  years (Livio and Pringle 1997), that would produce an episodic jet.

Recently, the magneto-hydrodynamical collimation has been reinforced by the detection of the magnetic field in the torus of the PN K3–35 (Miranda et al. 2001), which shows strong similarities with Hen 3–1475. It has a bipolar precessing jet and a dense equatorial toroid, and its jet is a strong source of [N II] emission (Miranda et al. 2000).

## 5. Conclusions

The luminosity ( $\sim 12600L_{\odot}$ ) derived assuming that the star is located at a distance of 5.8 kpc, the nitrogen overabundance derived from the spectroscopic data, the timescales estimated for the development of the observed morphology and the rest of the parameters analysed in this paper are all consistent with the classification of Hen 3–1475 as a relatively massive star ( $M \sim 3 - 5 M_{\odot}$ ) in the post-AGB phase, as previously suggested by R95.

One of the most remarkable results found in the analysis of this flow is the variation of the radial velocity along

the axis of the jet (see Sect. 3.3). We have shown above that the overall trend of the radial velocity with distance to the source can be explained as a result of a variable velocity ejection (maybe episodic mass loss events) together with a slowing down with distance along large scales due to the entrainment process and/or as a result of the drag forces of the ambient medium.

A scenario with a quasi-periodic variability (with timescales of  $\sim 100$  years) and a slow precession (with a period of  $\sim 1500$  years) would explain the formation of the knots, the observed morphology and the observed spectra of Hen 3–1475. Superimposed on the quasi periodic velocity variability there is an underlying trend of increasing velocity over time. The ejection velocity variability predicts a shock velocity which is significantly lower than the velocity obtained for the intermediate knots, as required to explain the spectra observed in these knots.

The periodic variability is most probably the consequence of quasi-periodic mass-loss events of very short duration experienced by the central star, of still unknown origin. In order to explain the observations, we can invoke instabilities in the mass outflow, the possible influence of a binary companion or coronal mass ejection-like induced by the magnetic field generated as a consequence of the dynamo action induced by the differential rotation between the rapidly rotating stellar core and the more slowly rotating envelope of the star.

The point-symmetric geometry displayed by Hen 3–1475 is most probably caused by the precession of the jet. It has been shown by different authors that precession requires the existence of a binary system, in which the wind, either from the central post-AGB star or from an accretion disk is magneto-hydrodynamically collimated. Otherwise, the precession could also be radiation-induced by the irradiation of the disk.

The emission lines of several knots show double-peaked profiles in both the intermediate and innermost knots, with a line width from  $\sim 475 \text{ km s}^{-1}$  up to  $1000 \text{ km s}^{-1}$  (see Sect. 3.4). The huge dispersion of velocities observed in these knots were interpreted as violent deceleration occurring in the knots by BH01. However, we have shown that these decelerations are unlikely to be caused by environmental drag. In the scenario we propose here, these knots are bow shock-like structures which contain a large range of velocities projected along the line of sight. In this way, we can explain how such an extremely wide double-peaked emission line profiles can be produced in a small volume.

*Acknowledgements.* AR is very grateful to E. de Gouveia Dal Pino, G. García-Segura, A. Raga and L. Binette for fruitful discussions and comments. We are grateful to Luc Binette for providing us the photoionization-shock code MAPPINGS Ic. AR and RE are partially supported by DGICYT grant PB98-0670 and by MCyT grant AYA2002-00205. MB was supported by STScI grant number GO-06364.03-A. This work was partially funded through grant PB97-1435-C02-02 from the Spanish Dirección General de Enseñanza Superior (DGES).

## References

- Binette L., Dopita M.A. & Tuohy I.R. 1985, ApJ 297, 476  
 Blackman E.G., Frank A., Markiel J.A., Thomas J.H. & van Horn H.M. 2001a Nature, 409, 485  
 Blackman E.G., Frank A. & Welch C. 2001b, ApJ 546, 288  
 Bobrowsky, M., Sahu, K.C., Parthasarathy, M., & García-Lario, P. 1998, Nature, 392, 469  
 Bobrowsky M., Zijlstra, A.A., Grebel, E.K., Tinney, C.G., te Lintel Hekkert, P., Van de Steene, G.C., Likkell, L., & Bedding, T.R. 1995, ApJ 446, L89  
 Bobrowsky, M. & Zipoy, D.M. 1989, ApJ, 347, 307  
 Borkowski K.J., Blondin J.M. & Harrington J.P. 1997, ApJ 482, L97  
 Borkowski K.J. & Harrington J.P. 2001, ApJ 550, 778 (BH01)  
 Bujarrabal V., Castro-Carrizo A., Alcolea J. & Sánchez Contreras C. 2001, A&A 377, 868  
 Cabrit S. & Raga A.C. 2000, A&A 354, 667  
 de Gouveia Dal Pino E. 2001, ApJ 551, 347  
 de Gouveia Dal Pino E. & Benz W. 1993, ApJ 410, 686  
 de Gouveia Dal Pino E. & Benz W. 1994, ApJ 435, 261  
 Deguchi S. 1977, in IAU Symp. 180 on *Planetary Nebulae*, ed. H.J. Habing & H.J.G.L.M. Lamers (Dordrecht: Kluwer), 151  
 Dopita, M.A., Binette L. & Tuohy I.R. 1984a, ApJ 282, 142  
 Dopita M. A., Binette L., Dodorico S. & Benvenuti P. 1984b, ApJ 276, 653  
 Eislöfel J., Mundt R. & Böhm K.-H. 1994, AJ 108, 1042  
 García-Lario P., Manchado A., Pych W. & Pottasch S.R. 1997, A&AS 126, 479  
 García-Segura, G. 1997, ApJ 489, L189  
 García-Segura, G., Langer, N., Rzyzyczka, M. & Franco, J. 1999, ApJ 517, 767  
 García-Segura, G. & López, J. A. 2000, ApJ 544, 336  
 García-Segura, G., López, J. A. & Franco, J. 2001, ApJ 560, 928  
 Harpaz A., Rappaport S. & Soker N. 1997, ApJ 487, 809  
 Hartigan P., Mundt R. & Stocke J. 1986a, AJ 91, 1357  
 Hartigan P., Lada C.J., Stocke J. & Tapia S. 1986b, AJ 92, 1155  
 Hartigan P., Raymond J. & Hartmann L. 1987, ApJ 316, 323  
 Hartigan P. & Raymond J. 1993, ApJ 409, 705  
 Heathcote S., Reipurth B. & Raga A.C. 1998, AJ 116, 1940  
 Hrivnak B.J., Kwok S. & Su K.Y.L. 2001, AJ 121, 2775  
 Kingsburgh, R.L. & Barlow M.J. 1994, MNRAS 271, 257  
 Knapp G.R., Bowers P.F., Young K. & Phillips T.G. 1995, ApJ 455, 293  
 Livio, M. & Pringle J.E. 1997, ApJ 486, 835  
 López R., Riera A., Raga A.C., Anglada G., López J.A., Noriega-Crespo A. & Estalera R. 1996, MNRAS 282, 470  
 Mastrodemos N. & Morris M. 1999, ApJ 523, 357  
 Meaburn, J., Wolstencroft, R. D., Raymond, J. C., Walsh, J. R., & Lopez, J. A. 1988, in *Dust in the universe; Proceedings of the Conference*, eds. M. Bailes and D. A. Williams Cambridge University Press, 381  
 Mellema G. 1995, MNRAS 277, 173  
 Miranda L. F., Fernández M., Alcalá J. M., Guerrero M. A., Anglada G., Gómez Y., Torrelles J. M., Aaquist O. B. 2000, MNRAS 311, 748  
 Miranda L. F., Gómez Y., Anglada G., Torrelles, J. M. 2001, Nature, 414, 284  
 Morse, J. A., Hartigan, P., Cecil, G., Raymond, J. C. & Heathcote, S. 1992, ApJ, 399, 231

- Morse, J. A., Heathcote, S., Cecil, G., Hartigan, P., & Raymond, J. C. 1993, ApJ, 410, 764
- Norman C.A. & Silk J. 1979, ApJ 228, 197
- Parthasarathy M. & Pottasch S.R. 1989, A&A 225, 521
- Raga A.C. 1991, ASP Conference Series 16, 247
- Raga A.C. & Biro S. 1993, MNRAS 264, 758
- Raga A.C. & Böhm K.-H. 1986, ApJ 308, 829
- Raga A.C., Böhm K.-H. & Cantó J. 1996, RMxAA 32, 161
- Raga A.C., Cantó J., Binette L. & Calvet N. 1990, ApJ 364, 601
- Raga A.C. & Kofman L. 1992, ApJ 386, 222
- Reipurth B., Raga A.C. & Heathcote S. 1992, ApJ 392, 145
- Riera, A., García-Lario P., Manchado A., Pottasch S.R. & Raga A.C. 1995, A&A 302, 137 (R95)
- Riera A., García-Lario P., Manchado A. & Bobrowsky M. 2001, in *Post-AGB Objects as a Phase of Stellar Evolution*, eds. R. Szczerba & S.K. Górný. Kluwer Academic Publishers, 209
- Riera A., García-Lario P., Manchado A., Bobrowsky M. & Estalella R. 2002, RMxAA (Serie de Conferencias) 13, 127
- Sánchez Contreras C. & Sahai R. 2001, ApJ 533, L173
- Schwartz R.D. 1978, ApJ 223, 884
- Shull J.M. & McKee C.F. 1979, ApJ 227, 131
- Solf J., Böhm K.-H. & Raga A.C. 1986, ApJ 305, 795
- Soker N. 1998, ApJ 496, 833
- Soker N. 2000, MNRAS 312, 217
- Soker N. & Livio M. 1994, ApJ 421, 219
- Stone J.M. & Norman M.L. 1993a, ApJ 413, 198
- Stone J.M. & Norman, M.L. 1993b, ApJ 413, 210
- te Lintel Hekkert P. 1991, A&A 248, 209
- Trammell, S.R. & Goodrich, R.W. 2002, ApJ, 579, 688
- Ueta, T., Meixner, M., Bobrowsky, M. 2000, ApJ, 528, 861
- Ziljstra A.A., Chapman J.M., te Lintel Hekkert, P., Likkle L., Comeron F., Norris R.P., Molster F.J., & Cohen R.J. 2001, MNRAS 322, 280